NASA/TM-2016-219363

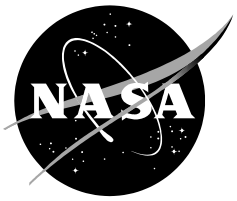

Direct Numerical Simulation of an Airfoil with Sand Grain Roughness on the Leading Edge

André F. P. Ribeiro, Damiano Casalino, and Ehab Fares
Exa GmbH, Stuttgart, Germany

Meelan Choudhari
Langley Research Center, Hampton, Virginia

October 2016

NASA STI Program ... in Profile

Since its founding, NASA has been dedicated to the advancement of aeronautics and space science. The NASA scientific and technical information (STI) program plays a key part in helping NASA maintain this important role.

The NASA STI program operates under the auspices of the Agency Chief Information Officer. It collects, organizes, provides for archiving, and disseminates NASA's STI. The NASA STI program provides access to the NTRS Registered and its public interface, the NASA Technical Reports Server, thus providing one of the largest collections of aeronautical and space science STI in the world. Results are published in both non-NASA channels and by NASA in the NASA STI Report Series, which includes the following report types:

- TECHNICAL PUBLICATION. Reports of completed research or a major significant phase of research that present the results of NASA Programs and include extensive data or theoretical analysis. Includes compilations of significant scientific and technical data and information deemed to be of continuing reference value. NASA counter-part of peer-reviewed formal professional papers but has less stringent limitations on manuscript length and extent of graphic presentations.

- TECHNICAL MEMORANDUM. Scientific and technical findings that are preliminary or of specialized interest, e.g., quick release reports, working papers, and bibliographies that contain minimal annotation. Does not contain extensive analysis.

- CONTRACTOR REPORT. Scientific and technical findings by NASA-sponsored contractors and grantees.

- CONFERENCE PUBLICATION. Collected papers from scientific and technical conferences, symposia, seminars, or other meetings sponsored or co-sponsored by NASA.

- SPECIAL PUBLICATION. Scientific, technical, or historical information from NASA programs, projects, and missions, often concerned with subjects having substantial public interest.

- TECHNICAL TRANSLATION. English-language translations of foreign scientific and technical material pertinent to NASA's mission.

Specialized services also include organizing and publishing research results, distributing specialized research announcements and feeds, providing information desk and personal search support, and enabling data exchange services.

For more information about the NASA STI program, see the following:

- Access the NASA STI program home page at http://www.sti.nasa.gov

- E-mail your question to help@sti.nasa.gov

- Phone the NASA STI Information Desk at 757-864-9658

- Write to:
  NASA STI Information Desk
  Mail Stop 148
  NASA Langley Research Center
  Hampton, VA 23681-2199

NASA/TM-2016-219363

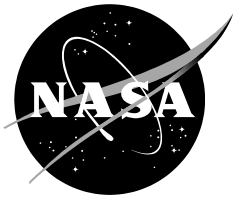

Direct Numerical Simulation of an Airfoil with Sand Grain Roughness on the Leading Edge

André F. P. Ribeiro, Damiano Casalino, and Ehab Fares
Exa GmbH, Stuttgart, Germany

Meelan Choudhari
Langley Research Center, Hampton, Virginia

National Aeronautics and
Space Administration

Langley Research Center
Hampton, VA 23681

October 2016

Acknowledgments

Computational resources for this work were provided by the NASA High-End Computing (HEC) Program through the NASA Advanced Supercomputing (NAS) Division at the Ames Research Center. The authors are grateful to Mattia Barbarino from CIRA, for the discussion about the semi-analytical trailing-edge noise model used in Section 3. One of the authors (MC) would like to acknowledge support from the NASA Advanced Air Transport Technology (AATT) and Transformational Tools and Technologies (TTT) projects. MC would also like to thank Dr. Florence Hutcheson of NASA Langley Research Center and Prof. Rodney Bowersox and Mr. Andrew Leidy of Texas A&M University for their extensive assistance with characterizing the surface roughness of installed trips on wind tunnel models. Thanks are also due to Prof. Holger Babinsky of Cambridge University for a useful technical discussion about boundary layer tripping in wind tunnel experiments.

Available from:

NASA STI Program / Mail Stop 148
NASA Langley Research Center
Hampton, VA 23681-2199
Fax: 757-864-6500

Abstract

As part of a computational study of acoustic radiation due to the passage of turbulent boundary layer eddies over the trailing edge of an airfoil, the Lattice-Boltzmann method is used to perform direct numerical simulations of compressible, low Mach number flow past an NACA 0012 airfoil at zero degrees angle of attack. The chord Reynolds number of approximately 0.657 million models one of the test conditions from a previous experiment by Brooks, Pope, and Marcolini at NASA Langley Research Center. A unique feature of these simulations involves direct modeling of the sand grain roughness on the leading edge, which was used in the abovementioned experiment to trip the boundary layer to fully turbulent flow. This report documents the findings of preliminary, proof-of-concept simulations based on a narrow spanwise domain and a limited time interval. The inclusion of fully-resolved leading edge roughness in this simulation leads to significantly earlier transition than that in the absence of any roughness. The simulation data is used in conjunction with both the Ffowcs Williams-Hawkings acoustic analogy and a semi-analytical model by Roger and Moreau to predict the farfield noise. The encouraging agreement between the computed noise spectrum and that measured in the experiment indicates the potential payoff from a full-fledged numerical investigation based on the current approach. Analysis of the computed data is used to identify the required improvements to the preliminary simulations described herein.

Introduction

Broadband noise generation due to the convection of turbulent boundary layer eddies over an airfoil trailing edge represents a generic source of noise that occurs in several technological applications such as the non-propulsive, i.e., airframe component of aircraft noise, turbomachinery noise, rotorcraft noise, and wind turbine noise. Trailing edge scattering enhances the weak, $O(M^8)$ acoustic power radiated by the quadrupole noise sources associated with turbulent eddies in free space to a substantially higher level that scales with M^5 at large Helmholtz numbers (i.e., for airfoil chord >> acoustic wavelength). For wind turbine blades, the trailing edge noise accounts for a dominant fraction of the overall acoustic radiation (Oerlemans et al., 2006). In airplane and rotorcraft applications, trailing edge noise is subdominant with respect to the other sources; however, as those sources are reduced in the future via the noise reduction concepts that are currently under development, the trailing edge noise will emerge as a significant contributor to the overall noise from the vehicle.

Prediction methods for trailing edge noise

Traditionally, trailing edge noise has been predicted using semi-analytical models based on formulations developed in the 1970s, starting from the pioneering works of Ffowcs Williams and Hall (1970), Howe (1978, 2001), Chase (1975), and Amiet (1976). The main difference between these formulations consists of the way the acoustic analogy is formulated to establish the dependence of the radiated acoustic field on the turbulent flow statistics. Ffowcs Williams and Hall made use of the properties of the turbulent velocity fluctuations near the trailing edge, whereas Amiet used the unsteady surface pressure field induced by the convected turbulence. Besides this formal difference, all of these formulations are based on the assumption that, in the range of frequencies associated with the Lighthill stress tensor due to boundary layer turbulence convecting past the trailing edge, the acoustic wavelength is sufficiently small in comparison with the airfoil chord so that the airfoil is acoustically equivalent to a semi-infinite plate.

More recently, Roger and Moreau (2005) have extended the Amiet formulation to take into account the effect of acoustic back-scattering near the leading-edge. The finite chord of the airfoil has a noticeable effect at low reduced frequencies, especially in the case of Fourier components of the vortical fluctuations that correspond to vorticity vectors that are skewed from the edge and thus have a subsonic trace velocity (subcritical components). Following the approach proposed by Schlinker and Amiet (1981), Rozenberg et al. (2008), among others, have applied the finite-chord trailing edge noise model to compute the noise from rotating blades. This work was performed under the assumption of sufficiently small rotation frequencies in comparison with the characteristic frequencies of trailing edge noise. Amiet-based semi-analytical formulations constitute the state of the art in the prediction of trailing edge noise for both static and rotating airfoils. However, in order to be used as predictive methods, they require the wall pressure spectrum in proximity of the trailing edge. The wall pressure fluctuations beneath a turbulent boundary layer are induced by turbulent eddies with a broad range of scales and convected at different speeds at different distances from the wall. A crude but effective simplification of such a complex phenomenology consists in subdividing the dynamic range into two parts, one related to the so-called inner layer of the boundary layer, the viscous sublayer, and the other one related to the outer part. Each layer is characterized by its own characteristic velocity and length scales.

Following Chase (1980) and Howe (1998), the dynamics of the inner layer can be reduced by using the friction velocity and the displacement thickness, whereas Amiet used the boundary-layer edge velocity and the displacement thickness. In both models, the frequencies are reduced by displacement thickness and edge velocity. As shown by Keith et al. (1992), the inner and outer layer variables provide a better collapse of the wall pressure spectrum at high and low frequencies, respectively. Based on this observation, Goody (2004) modified the Chase-Howe model by introducing a term related to the ratio between the inner and the outer time scales, and by including an additional term to account for the experimentally observed decay of ω^{-5} as $\omega \to \infty$. In addition, the boundary layer thickness, instead of the displacement thickness, was used to reduce the frequencies, under the assumption that the size of the large coherent eddies scales with the

boundary layer thickness. More recently, Goody's model has been modified by Rozenberg et al. (2012) to account for the presence of adverse pressure gradients. The model was successfully assessed by using six experimental data sets and was subsequently used in conjunction with Roger and Moreau's model to predict the trailing-edge noise for an NACA-0012 airfoil. Comparisons with the noise measurements by Brooks and Hodgson (1981) revealed a significant improvement when the pressure gradient correction is used in Goody's wall pressure model.

Trailing-edge noise models based on a combination of semi-analytical solutions for scattering near the airfoil trailing edge and semi-empirical models for the surface pressure spectrum in the proximity of the trailing edge are routinely used to compute the self-noise of rotating machines ranging from cooling fan systems (Rozenberg et al., 2008) to wind turbines (Bertagnolio, 2012). However, these models involve uncertainties related to the semi-analytical nature of the acoustic radiation model when the blades cannot be approximated by zero-thickness flat plates, and to the accuracy of the wall pressure model when the blades are operated outside the range of the empirical calibration. In practice, the accuracy of the semi-empirical prediction models is limited by the prevalent uncertainty in the measurements of trailing edge noise used to calibrate them (Herr et al. 2013, 2015).

A synergistic combination of advanced measurements and numerical simulations may help lower these uncertainties and the use of a validated simulation database can provide an additional means of calibrating and improving the semi-analytical/empirical models. The analytical models encounter additional difficulties with an accurate estimation of the effects of trailing edge noise treatments such as serrations (Dassen et al., 1996), slits (Gruber et al., 2010), and brushes (Herr and Dobrzynski, 2005). Therefore, high-fidelity numerical simulations can be used to shed light on the underlying mechanisms responsible for noise reduction and the subsequent design and optimization of noise reduction devices. Herr et al. (2015) provide a partial overview of representative numerical simulations and their comparison with some of the best available measurements of trailing edge noise for both symmetric and cambered airfoils that were selected for the BANC series of workshops hosted by the AIAA (Choudhari et al. 2016).

Computational predictions of airfoil self-noise typically employ a hybrid approach based on the simulation of unsteady flow near the airfoil, which then provides the input for an acoustic analogy type calculation that propagates the nearfield information to predict the far field noise. Computational methodologies used for the nearfield flow include, in the order of increasing fidelity: CAA computations based on a synthetic source distribution derived from a RANS solution for the time-averaged flow over an airfoil (Ewert et al., 2009), wall-modeled LES (Wolf and Lele, 2012, George and Lele, 2016), hybrid RANS-LES (Iob et al., 2014), wall-resolved LES (Manoha et al., 2000, Oberai et al., 2002, Marsden et al., 2008, Gloerfelt and Le Garrec, 2009, and Lin et al., 2013), and DNS (Jones at al., 2010, Sandberg and Jones, 2015).

The DNS simulations do not involve any approximations related to the smaller scales of unsteady motion, and hence, can be particularly valuable for trailing edge noise. The DNS of airfoil self-noise by Sandberg and Jones (2015) were limited to a Reynolds number of 50,000. In contrast, the typical laboratory experiments targeting broadband noise due to turbulent boundary layers approaching the airfoil trailing edge correspond to Reynolds numbers in excess of approximately 0.5 million (see, for instance, Brooks et al., 1989 and Herrig, 2011). Even though simulations based on wall-modeled LES and hybrid RANS-LES have been performed at Reynolds numbers of 0.5 million and above, their inability to model the near wall eddies is known to result in significant errors in predicting the intermediate to high frequency portion of the surface pressure spectrum (i.e., for $f > f_I$, where the subscript I corresponds to the integral scale of turbulence) as shown by the work by Park and Moin (2016). Thus, there is a strong need to extend the DNS predictions to higher Reynolds numbers.

Role of boundary layer tripping

Both the level and the spectral distribution of the acoustic field radiated from the airfoil are functions of the boundary layer thickness just upstream of the trailing edge, which in turn depends on the location of laminar-turbulent transition in the boundary layer flow. To minimize the sensitivity of the transition process to the details of the freestream disturbance environment, boundary layer tripping is often used to ostensibly fix the transition location and to ensure an easier to reproduce, fully turbulent boundary layer flow ahead of the trailing edge location. However, despite many decades of employing boundary layer trips in wind tunnel experiments, trip design continues to be an empirical art rather than science, which can lead to considerable variability in transition location and hence in the boundary layer parameters near the trailing edge. Due to the uncertainty in determining optimal trip parameters for a given application, conservative trip designs, i.e., larger than necessary trip heights are often used to ensure transition within the short distance behind the trip. The over tripping of the boundary layer flow can also add to the uncertainty in boundary layer thickness immediately behind the trip, as well as introducing a spanwise distortion of the mean flow in the wake. For deterministic trips such as zigzag tapes, over tripping can introduce strong periodic structures in the boundary layer flow that can persist for long distances into the trip wake, even after the flow has become fully turbulent. Trip induced flow distortion can potentially influence the trailing edge noise, and there is experimental evidence that trips may result in an additional source of noise associated with the interaction of unsteady vorticity structures in the transitional boundary layer with the surface deformation associated with the trips.

These extraneous mechanisms add further to the variability due to transition location among the different measurements of the same airfoil geometry at similar flow conditions. In particular, phased microphone array measurements by Hutcheson and Brooks (2002) have shown that scrubbing noise due to grit near the leading edge can overpower the trailing edge noise at higher frequencies. The grit-induced noise had been filtered out in the earlier measurements (Brooks and Hodgson, 1981, Gershfeld et al., 1988), since they used the Coherent Output Power (COP) method, which is based on a cross-spectral analysis of pairs of output signals from microphones placed around the model airfoil. Acoustic measurements of the NACA 0012 airfoil by Migliore and Oerlemans (2003) also indicated peculiar discrepancies with the measurements by Brooks, Pope, and Marcolini (1989). Again, differences in tripping and acoustic measurement techniques were suggested as possible reasons behind these discrepancies.

Transition prediction and CFD simulations

To avoid the variability associated with the boundary layer history upstream of the trailing edge, numerical simulations of the unsteady nearfield must mimic the tripping configuration in the experiment. Eventually, validated numerical simulations of this type would be useful in designing optimal trips that accomplish their targeted function with minimal parasitic drag and extraneous distortion of the downstream flow. Modeling the transition process within the CFD computation is also important in purely aerodynamic simulations. According to the CFD Vision 2030 of the NASA Revolutionary Computational Aerosciences (RCA) subproject (Slotnick et al., 2014), the most critical area in computational fluid dynamics (CFD) simulation capability that will remain a pacing item in the analysis and design of aerospace systems by 2030 is the ability to adequately predict viscous turbulent flows with boundary layer transition and flow separation. Specifically, physics-based predictive capability for boundary layer transition is one of the important set of capabilities required for satisfying the requirements outlined in Vision 2030 CFD. Presently, many CFD design processes include an estimation of boundary layer transition based on models ranging in fidelity from purely empirical to semi-empirical ones based on the amplification of hydrodynamic instability waves. Because of the complexity of the transition process and its sensitivity to disturbance environment, no generalized transition prediction capability is in widespread use in Navier-Stokes CFD and the commonly adopted approach is running such codes in a fully turbulent mode without any transition modeling. When transition is simulated in lieu of being modeled, the number of cells within

the laminar and transitional regions is 10 to 100 times larger than that in the turbulent region. Therefore, the cost of simulating the transitional region has been identified as a major bottleneck to high fidelity computations in aerospace applications.

In the context of subscale wind tunnel experiments, boundary layer tripping is most commonly accomplished via mechanical trips in the form of 2D trip wires (Garcia-Sagrado and Hynes, 2012), 3D but deterministic zigzag tapes (Herrig, 2011), or distributed roughness in the form of grit (Brooks et al., 1989). On the other hand, nearly all previous numerical simulations involving intentional boundary layer tripping have used artificial, numerical trip devices such as localized suction and blowing (Wolf and Lele, 2012, George and Lele, 2016) or, in the context of hybrid RANS-LES computations, treated the boundary layer flow as fully turbulent, effectively allowing the RANS model to predict the transition location. The only exception to this practice appears to be the LES by Winkler et al. (2009), which used an array of triangular-planform trips mounted within the front portion of the airfoil to trip the boundary layer. In comparison with the triangular trips, the nominally stochastic pattern of surface mounted grit or sand grain roughness is likely to reduce the flow distortion in the fully turbulent region and is often used during subscale tests in lieu of a deterministic trip. Distributed roughness of this type can also occur naturally in aerodynamic applications, either as a result of degradation of the surface over time or due to manufacturing imperfections or, in the case of hypersonic vehicles, arises as a byproduct of surface ablation due to aerodynamic heating of the vehicle surface. Current modeling of distributed-roughness effects is primarily empirical and no single correlation appears to capture all of the relevant physics for both engineered and service-related roughness. Therefore, simulations are needed to enhance the understanding of transition mechanisms so that physics-based predictive models can be developed and validated in detail. Because of the geometric complexity of sand grain roughness, modeling the flow over an airfoil with grit has not been investigated thus far.

The objective of the present work is to compute trailing edge noise for an experimental configuration where the airfoil boundary layer was tripped by sand grain roughness in the vicinity of the leading edge. To that end, the nearfield computations target the DNS of an NACA 0012 airfoil at zero degrees of incidence and a chord Reynolds number of 0.657 million. The flow conditions and the trip configuration are based on the experiment of Brooks and Hodgson (1981), whose classic work provided the first experimental validation of trailing edge noise theories. Natural transition is first computed on the clean airfoil, followed by simulations on the same airfoil with grid-resolved spheres scattered over the leading edge to reproduce the grit present in the aforementioned experiments. Trailing edge noise is computed in the nearfield and extrapolated to the farfield using different methods. The remaining parts of this report are organized as follows. Section 1 briefly describes the Lattice-Boltzmann method (LBM) as implemented in version 5.3b of the commercial software PowerFLOW®, which is used for all of the simulations described here. The near wall discretization methodology implemented within PowerFLOW has the built-in capability to mesh small-scale details associated with the grit and still run efficiently and facilitate various types of postprocessing using a variety of tools. Hence, it has certain advantages for studying roughness-induced transition. Section 2 provides an overview of the flow configuration and the simulation setup. Section 3 describes the results obtained from the computations and their comparison with the experimental data. Conclusions are presented in section 4.

Nomenclature

b_c = spanwise correlation coefficient
c = airfoil chord
C_i = collision term
C_p = pressure coefficient
f = frequency
f_i = particle density function
f_i^{eq} = particle equilibrium distribution
k = roughness height equivalent to one half of mean particle diameter
M = Mach number
r = distance to microphone
Re = Reynolds number
s_e = experimental airfoil span
s_s = simulation airfoil span
t = time
T_0 = temperature
U = freestream velocity
x = streamwise position
y = surface normal position
y^+ = non dimensional wall distance
z = spanwise position

δ = boundary layer thickness
δ^* = boundary layer displacement thickness
λ_2 = quantity used for vortex detection
θ = boundary layer momentum thickness
ρ = fluid density
τ = relaxation time
ω = turbulence decay
ω_i = weight function

$\mathbf{c}$ = particle velocity vector
$\mathbf{u}$ = fluid velocity vector
$\mathbf{x}$ = position vector

DNS = Direct Numerical Simulation
FW-H = Ffowcs Williams-Hawkings
LBM = Lattice-Boltzmann method
LES = Large Eddy Simulation
PSD = power spectral density
R&M = Roger and Moreau
RANS = Reynolds-Averaged Navier-Stokes
RMS = root mean square
T-S = Tollmien-Schlichting
TE = trailing edge

1. Numerical Method

The Lattice-Boltzmann equation has the following form (Chen et al., 1997, Chen and Doolen, 1998):

$$f_i(\vec{x} + \vec{c}_i\Delta t, t + \Delta t) - f_i(\vec{x}, t) = C_i(\vec{x}, t) \tag{1}$$

where f_i is the particle density function, which represents the probability for particles to travel with speed **c** from the position **x** at time t in the direction i. The travel speed is chosen so that particles travel one cell in one time step, effectively making the CFL number (Courant et al., 1928) for f_i equal to one. The collision term C_i is modeled with the well-known BGK approximation (Bhatnagar et al., 1954) as follows:

$$C_i(\vec{x}, t) = -\frac{1}{\tau}\left[f_i(\vec{x}, t) - f_i^{eq}(\vec{x}, t)\right] \tag{2}$$

where τ is the relaxation time, which relates to the fluid viscosity ν with the relation $\nu=a\,(\tau-\Delta t/2)$, where a is the speed of sound and Δt is the time step. The term f_i^{eq} is the equilibrium distribution, which is approximated by a third order expansion (Fan et al., 2006):

$$f_i^{eq}(\vec{x}, t) = \rho\omega_i\left(1 + \frac{\vec{c_i}\cdot\vec{u}}{T_0} + \frac{(\vec{c_i}\cdot\vec{u})^2}{2T_0^2} - \frac{\vec{u}^2}{2T_0} + \frac{(\vec{c_i}\cdot\vec{u})^3}{6T_0^3} - \frac{(\vec{c_i}\cdot\vec{u})\vec{u}^2}{2T_0^2}\right) \tag{3}$$

where ρ is the fluid density, ω_i is the weight function, which depends on the direction being calculated, **u** the fluid velocity, and T_0 the temperature, which is set to 1/3, in lattice units, for isothermal cases (Chen and Teixeira, 2000). To recover the fluid quantities from f_i, the Chapman-Enskog expansion is employed (Chapman and Cowling, 1990), which yields:

$$\rho(\vec{x}, t) = \sum_i f_i(\vec{x}, t), \qquad \rho\vec{u}(\vec{x}, t) = \sum_i \vec{c}_i f_i(\vec{x}, t) \tag{4}$$

PowerFLOW 5.3b solves the D3Q19 (3 dimensions, 19 velocity states) formulation of the Lattice-Boltzmann equation for direct numerical simulations (DNS). This has been demonstrated to correspond to solving the Navier-Stokes equations (Chen et al., 1992, Qian et al., 1992, Shan et al., 2006) at the continuum limit. The interaction of a laminar boundary layer with a grit strip and the consequent transition to turbulence requires a level of spatial and temporal resolution that is compatible with DNS. Hence the turbulence modeling capability of PowerFLOW (Chen et al., 2003) is not used for the present simulations.

The LBM is solved on a grid composed of cubic volumetric elements (voxels). A variable resolution by a factor of two is allowed between adjacent regions. Consistently, the time step is varied by a factor two between two adjacent resolution regions. Solid surfaces are automatically facetized within each voxel intersecting the wall geometry. This facetization creates planar surface elements, named surfels (Chen et al., 1998). Time advancement is performed with an explicit scheme, which allows for efficient, highly-scalable simulations.

Pressure fluctuations in the nearfield are directly resolved by the solver (Brès et al., 2009), but in order to allow for coarser grids in the farfield, a Ffowcs Williams-Hawkings (FW-H) computation is performed, based on Farassat's formulation 1A (Farassat and Succi, 1983) and a forward-time solution (Casalino, 2003).

The numerical methods described have been extensively validated for a wide variety of applications. Relevant to this study are other direct numerical simulations (Li et al., 2004), including trailing edge noise at lower Reynolds numbers with transition being triggered by a laminar separation bubble (Sanjosé et al., 2014). In addition, the current methodology has also been used for several applications at higher Reynolds numbers with turbulence modeling. This includes aerodynamic simulations of airfoils (Ribeiro et al., 2016) and full wings (Koenig et al., 2016), and aeroacoustics of full aircraft (Casalino et al., 2012).

2. Simulation Setup

The simulations presented herein model the NACA 0012 airfoil from the experiments by Brooks et al. (1989), consisting of a chord length of 304.8 mm and a trailing edge (TE) thickness of 0.1143 mm, which is referred to as the sharp TE airfoil. A chord Reynolds number of Re=0.657 million was chosen with a freestream temperature of 288 K. To limit the cost of the simulation, the Mach number is increased from an actual value of 0.093 to 0.1155. Simulations at M=0.093 would require a linear refinement factor of 1.22, or an increase in computational cost of 2.2. Experimental results for farfield noise are available for both Mach numbers, hence the data corresponding to M=0.1155 is used for initial comparisons, even though that means using a different Reynolds number for comparisons. This uncertainty is addressed in section 3. Boundary layer properties are available as equations based on the Reynolds number, hence the simulation Reynolds number is used to compute them. The simulation domain has a span of 1.875% of the airfoil chord, which corresponds to about 50 times the trailing edge thickness and about 60% of the local boundary layer thickness near the trailing edge in the tripped case. The farfield boundary conditions are located 35 chords away from the center of the profile.

The experiments use a commercial grit #60 over the first 20 percent of the airfoil chord on both top and bottom sides. The mean particle diameter is 0.29 mm and the packing density over the airfoil surface is specified as 3.8 particles/mm . This grit is approximated in the simulations by a distribution of spheres with a mean sphere diameter equal to the mean particle size and the same packing density as that in the experiment. Also, due to a lack of information concerning the distribution of particle size in the experiment, the particle diameter is assumed to have a Gaussian distribution with a standard deviation of 5% of the sphere diameter and the spheres are assumed to penetrate the airfoil surface by half a diameter (corresponding to an adhesive layer of one half diameter in thickness, although the adhesive layer itself is not modeled in the simulation), plus or minus a standard deviation of 5% of the sphere diameter. The spherical particles are first scattered over the surface homogeneously, but then shifted in span as well as in chordwise direction with a Gaussian distribution with a standard deviation of 1 sphere diameter. Approximately 12 spheres are present over the spanwise width of the computational domain. The discrete representation of the rough surface at a specified resolution level converts the spheres to a faceted representation (approximately 28 facets over the top half of each sphere), not unlike the shape of the abrasive grit particles. Each individual particle is oriented (i.e., rotated around its center) randomly.

The finest elements of the volume mesh are located on the leading and trailing edges of the airfoil. The finest element size is 0.002% of the chord, which corresponds to 30 voxels per sphere diameter, 15 voxels across the trailing edge thickness, 768 voxels per span, and an average y^+ of 0.5 over the airfoil. The grid was constructed so that the boundary layer fits inside the two finest regions, followed by quick coarsening after that. The leading edge region including the grit and the volume mesh is shown in Figure 1. For the simulation with grit over the airfoil leading edge, there are approximately 45 voxels across the mean boundary layer at the midpoint of the roughness patch on each side (i.e., at x/c = 0.1, where $\delta \approx 0.0009$c = 1.9k, where k denotes one half of the mean particle diameter). Similarly, there are approximately 300 voxels across the boundary layer thickness near the onset of boundary layer transition near x/c = 0.5, where $\delta/c \approx$ 0.006) and 1350 voxels near the airfoil trailing edge (x/c = 1, where $\delta/c \approx 0.027$). The case with the grit has a total of 8.69 billion voxels and 30.83 million surfels.

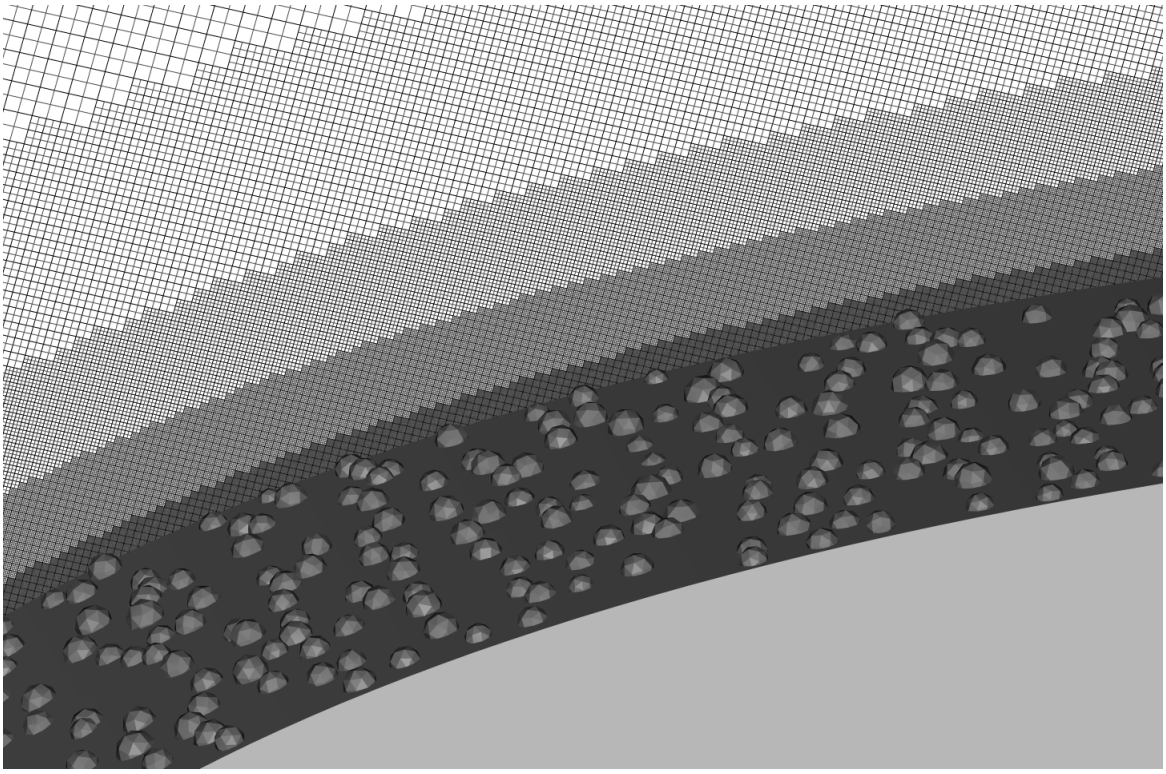

Figure 1. Surface of the airfoil near the leading edge with the grit and a plane at the periodic boundary showing the computational mesh.

The simulations are run for about 8 flow passes, which corresponds to about 0.06 seconds. Each flow pass takes about 260,000 CPU hours, which is equivalent to 111 wall clock hours on the 5040 cores used for each simulation. Only the second half of the simulation is used for computing turbulence statistics (corresponding to approximately 150 $\delta(x/c = 1.0)/U$ for the case with grit), i.e., the initial transient requires about 4 flow passes. The spectral analyses are done with single sided (i.e., times 2) spectra, computed with Hanning windows with a 50% overlap and a bandwidth of 127 Hz, which corresponds to averaging over 7 windows.

Preliminary simulations were carried out to verify that the setup is robust enough to run the very large computations. Initially, a semi-infinite flat plate was run to determine if the solver was able to achieve fully laminar flow up to a Reynolds number of 1 million when no forcing mechanism was present (e.g., upstream turbulence or acoustic disturbances associated with TE noise). These simulations did not generate turbulent flow, but did show velocity fluctuations on the flat plate leading edge and on the outlet boundary condition. The fluctuations were 6 orders of magnitude smaller than the freestream velocity and were discovered to be caused by truncation errors in the single precision code. To avoid them, the flow was simulated again, but using double precision. This reduced the fluctuations to 8 orders of magnitude smaller than the freestream velocity, which was deemed acceptable. The boundary layer profile was then measured in several stations along the plate and shown to be both self-similar and matching the Blasius solution, adding a quantitative validation of the flow field itself.

These studies were followed by simulations of the NACA 0012 airfoil with a symmetry plane going through the airfoil chord. The purpose of these simulations was to verify that the boundary layer would be entirely within the finest region of the mesh. The advantage of simulating this with a symmetry plane is that the simulation cost is cut in half, both in terms of CPU hours and memory requirements. The mesh was adjusted based on these simulations and the full simulations that followed are described in the next section.

3. Simulation Results

This section is divided into the aerodynamic results related to laminar to turbulent transition and acoustic results related to the boundary layer fluctuations and TE noise. The case of the clean airfoil with no boundary layer tripping is referred to as "clean", while the case with LE roughness is referred to as "grit".

Transition prediction

Figure 2 shows the distribution of time and spanwise average pressure coefficient (C_p) over the airfoil, compared with prediction based on the XFoil code (Drela, 1989). An excellent agreement is observed between both predictions, except for the bump in the XFoil result near 75% chord, which is attributed to the onset of laminar-turbulent transition in the XFoil data. While the clean case seems to show some curvature around the same region, subsequent results will show that the grit case transitions around 55% of the chord. The slight curvature seen in the grit case at 20% chord is the end of the roughness region.

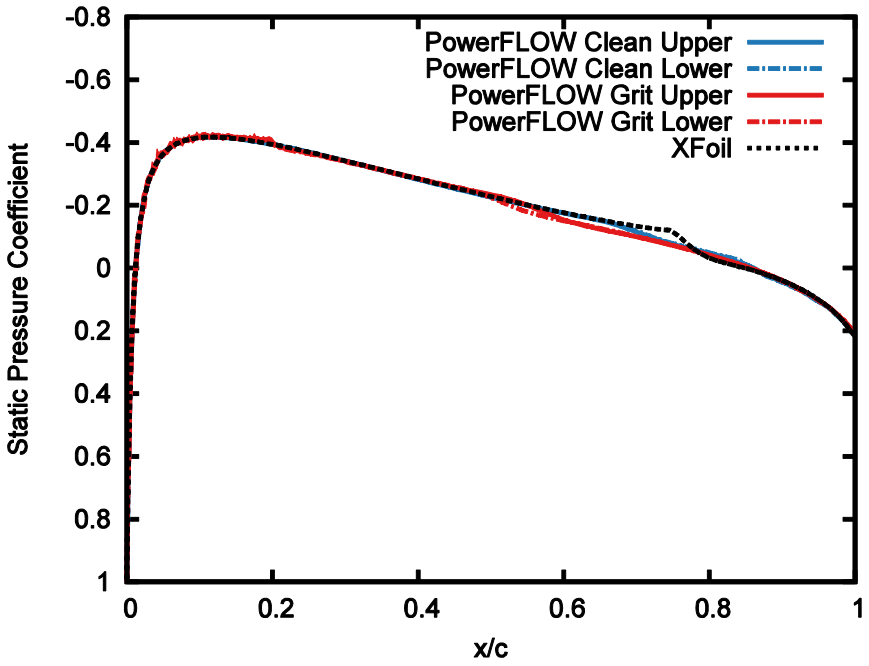

Figure 2. Surface pressure coefficient.

Figure 3 shows the upper mid-plane mean boundary layer thickness (δ), displacement thickness (δ^*), and momentum thickness (θ) compared to XFoil, experiments of Brooks et al. (1989), which are only available near the TE, and RANS computations of Casalino and Barbarino (2011), where transition was calculated using the transitional SST model (Langtry and Menter, 2009). The value of δ is calculated by measuring the wall-normal distance up to the location of maximum velocity inside the boundary layer. This is done for all points but x/c=1, where there is no local maximum, and therefore, δ is taken as the wall-normal distance to the inflection point in the velocity profile as requested in the problem statement for the BANC workshop (Herr et al., 2013, 2015). The change in edge detection criterion accounts for the kink in the curve around x/c=0.9. The δ values determined in this manner were used to estimate the integral thickness parameters δ^* and θ in the usual manner as described by Schlichting and Gersten (2000). In the laminar regions, the agreement of DNS results for δ^* and θ with predictions from XFoil and partially-laminar RANS calculations is excellent. The RANS results reach transition around 35% of the chord, which is significantly earlier than the results of numerical simulations for both clean and grit cases. The differences in various predictions of the boundary layer thickness parameters near the TE are mostly attributed to the different transition points for each case (and the effects of upstream history of the boundary layer in the case with

the grit). The boundary layer properties exhibit a rapid variation near the trailing edge; hence, differences with experiments could be due to the high sensitivity to exact surface location within this region. Lastly, differences in trip relative to that in the experimental configuration could also account for the differences in the overall evolution of the boundary layer properties, including their effect on boundary layer transition. Subsequent communications with Dr. Florence Hutcheson at the NASA Langley Research Center and Prof. Rodney Bowersox and Mr. Andrew Leidy at Texas A&M University have indicated that the adhesive layer used to attach the grit to the airfoil surface is much thinner than that assumed here, so that the assumed sphere penetration of half a sphere diameter corresponds to a significant underprediction of the trip height relative to the experiments of Brooks et al. (1989). The sensitivity of the flow to such changes will be the subject of future work.

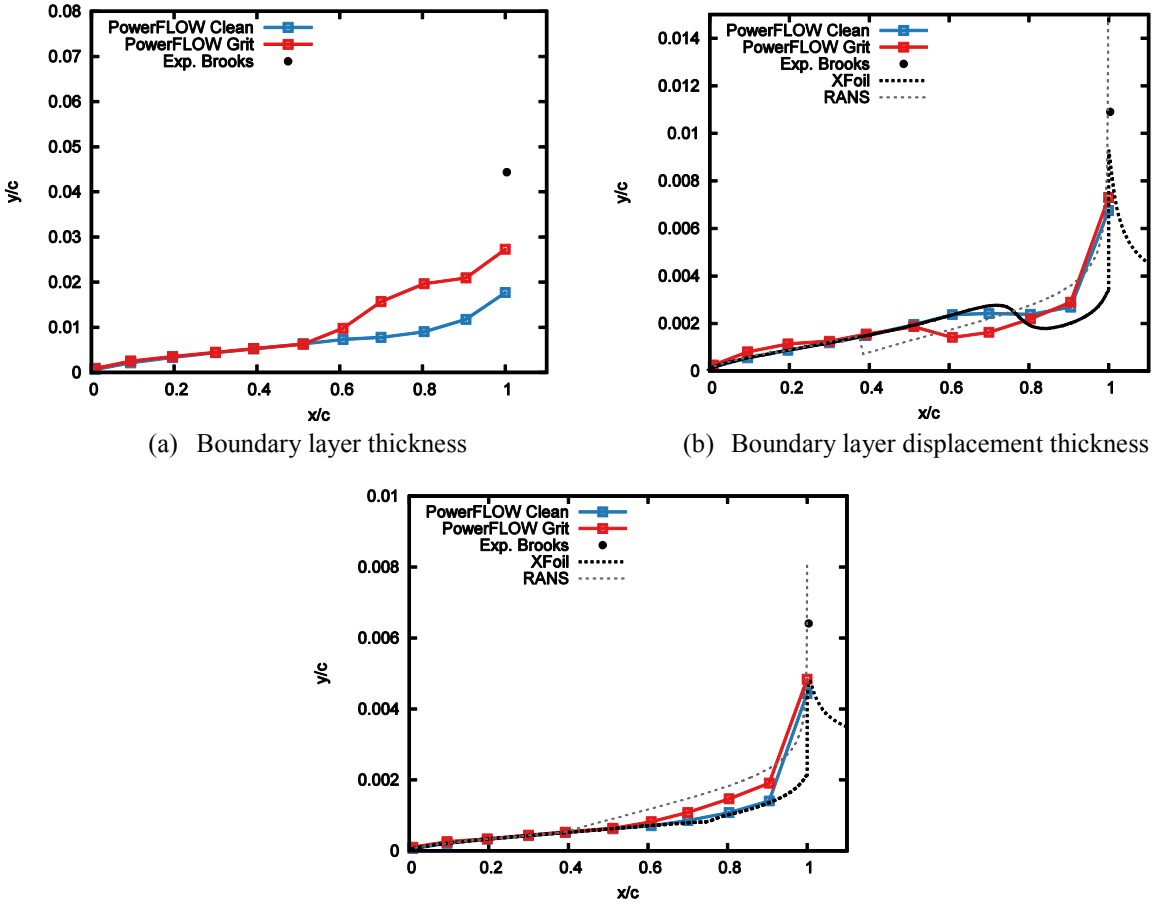

(a) Boundary layer thickness

(b) Boundary layer displacement thickness

(c) Boundary layer momentum thickness

Figure 3. Boundary layer properties.

Figure 4 shows chordwise distributions of both the mean skin friction coefficient and the standard deviation (i.e., RMS of fluctuations) C_p, both averaged along the span. The differences between the top and bottom of the airfoil surface for the grit case can be due to the simulation not running long enough or because the grit is not perfectly symmetric. Once again, the laminar results agree very well with the results based on both XFoil and the RANS equations. The numerical simulations for both clean and grit cases indicate a smooth rise in skin friction. The transition prediction in XFoil is calibrated to a typical disturbance environment at high altitudes. In contrast, the clean case does not include any free-stream unsteadiness besides (the very low) numerical noise, which would explain the later onset of transition relative to the XFoil predictions. The single precision case with a symmetry plane mentioned at the end of section 2 is also plotted for reference. Interestingly, the transition location is not significantly influenced by the symmetry plane, with the onset of transition for the symmetric case being in between the transition locations

along the upper and lower surfaces in the full case. However, the skin friction near the TE in the symmetric simulation is different from the full case, possibly because the TE flow cannot be captured properly by the symmetric simulation, although the mean pressure coefficient was perceived to be nearly identical in that region for the two cases. The root mean square of C_p fluctuations in the clean case is significantly higher than that in the grit case. The reason behind this discrepancy remains unclear, but it could be related to potential differences in transition mechanisms as well as the possibility that the boundary layer turbulence in the clean case does not reach a quasi-equilibrated state and the high wall pressure fluctuation levels are indeed due to a highly intermittent behavior. This can be also deduced by observing that the root mean square of C_p and the skin friction are not proportional, as expected for a turbulent boundary layer.

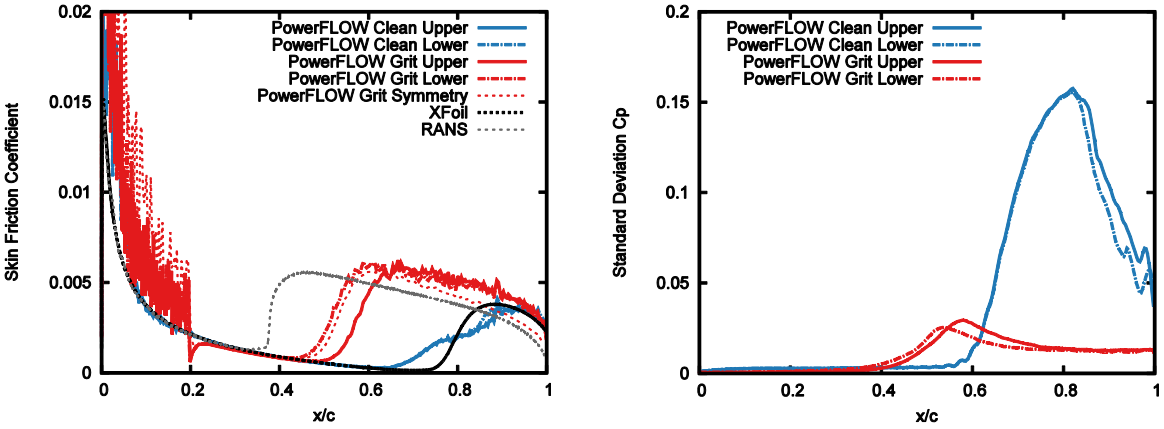

(a) Skin friction coefficient distribution

(b) Standard deviation pressure coefficient distribution

Figure 4. Surface distributions of indicating transition location.

Flow visualizations for both clean and grit cases are considered next. Figure 5 shows the isosurfaces of λ_2 (Jeong and Hussain, 1995), colored by velocity magnitude. These shed some light on the mechanism behind transition. For the grit case, two-dimensional flow structures form immediately after the grit and become stronger in the course of downstream propagation, indicating that they probably denote instability modes of the boundary layer flow. These waves quickly become three-dimensional and break down into short-scale structures suggestive of boundary layer turbulence. For the clean case, no instabilities are seen up to about the first half of the airfoil chord. What seem to be Tollmien-Schlichting (T-S) waves form and propagate along the chord. These waves then grow to become vortices that are still two-dimensional. Only near the TE, when the vortices have grown in size, do they become turbulent. In a wind tunnel experiment, the presence of free-stream turbulence is likely to modify the evolution of the 2D structures and probably lead to an earlier onset of transition than that in the numerical simulation of the clean case.

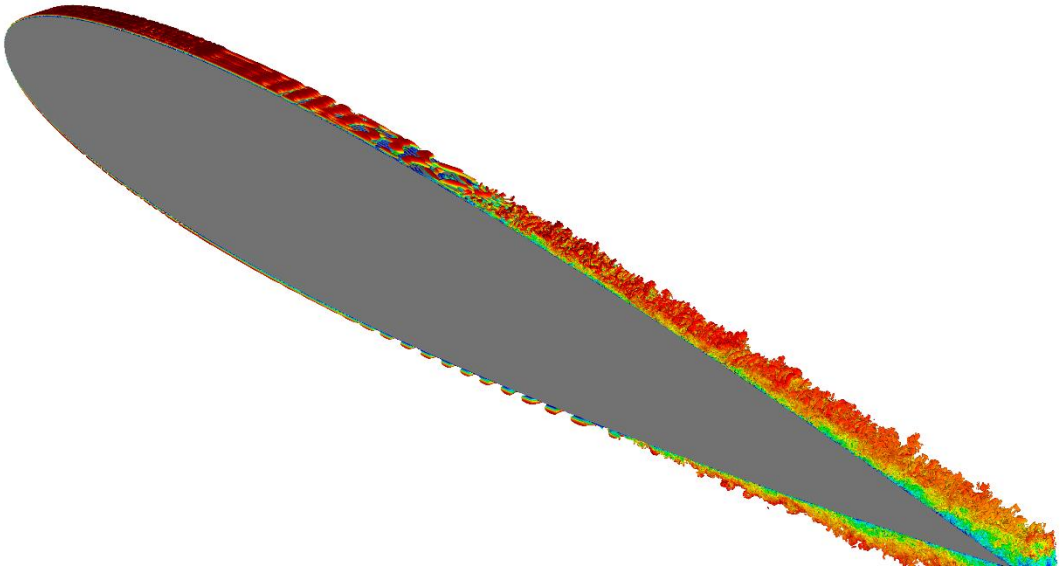

(a) Airfoil with grit

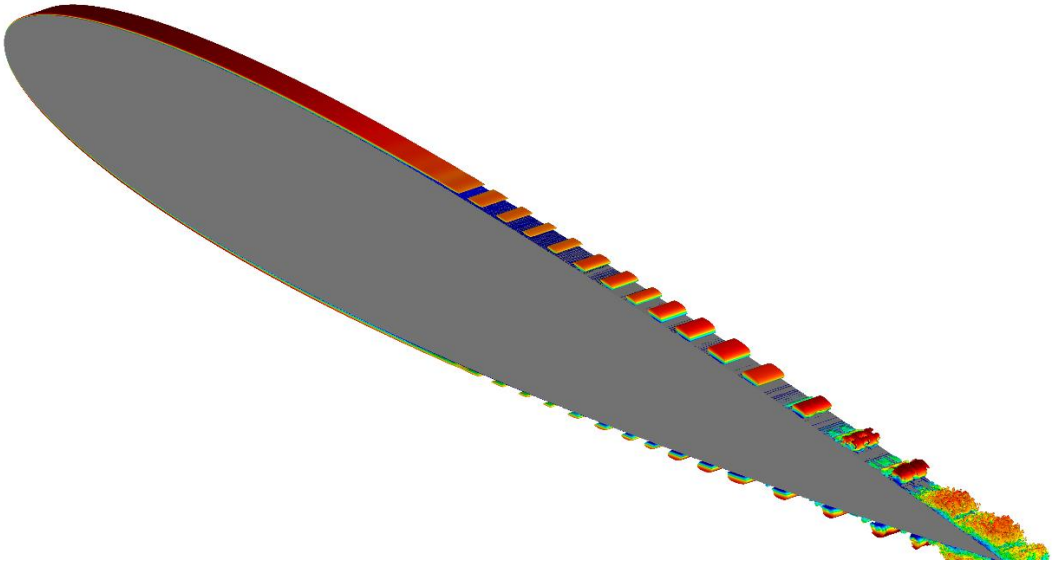

(b) Clean airfoil

Figure 5. Isosurfaces of λ_2 colored by velocity magnitude.

Figure 6 shows wall-normal profiles of RMS velocity fluctuations in the boundary layer. As seen in Figure 6(c), the velocity fluctuations in the laminar region are at most on the order of 10^{-4}. The dual peak nature of fluctuation profiles within the laminar portion of the clean case (Figure 6(b)) is rather reminiscent of the mode shapes of the T-S waves. However, the profiles in the grit case are somewhat different, possibly because of the influence of the grit on the mean boundary layer flow. For both clean and grit cases, the velocity fluctuations achieve their global peak significantly upstream of the trailing edge. The grit case shows a local overshoot in fluctuation amplitude over the grit region; the fluctuation amplitude reduces to O(0.001) behind the grit region, before beginning to rise again. At the onset of transition somewhat upstream of $x/c = 0.5$, the fluctuation amplitude is approximately 1 to 2 percent of the freestream velocity. Figure 6(c) indicates that, apart from the overshoot in the grit case, the chordwise amplification of the peak fluctuation amplitude across the pretransitional and transitional regions is similar in both the grit and the clean cases. Similar to the comparison of peak pressure fluctuations in Figure 4(b), the peak velocity fluctuation in the clean case is larger than that in the grit case. However, the increase in pressure fluctuation

amplitude in Figure 4(b) is significantly higher than the increase in velocity fluctuation in Figure 6(c), possibly as a result of increased spanwise coherence of the quasi-2D eddies in the clean case (Figure 5(b)).

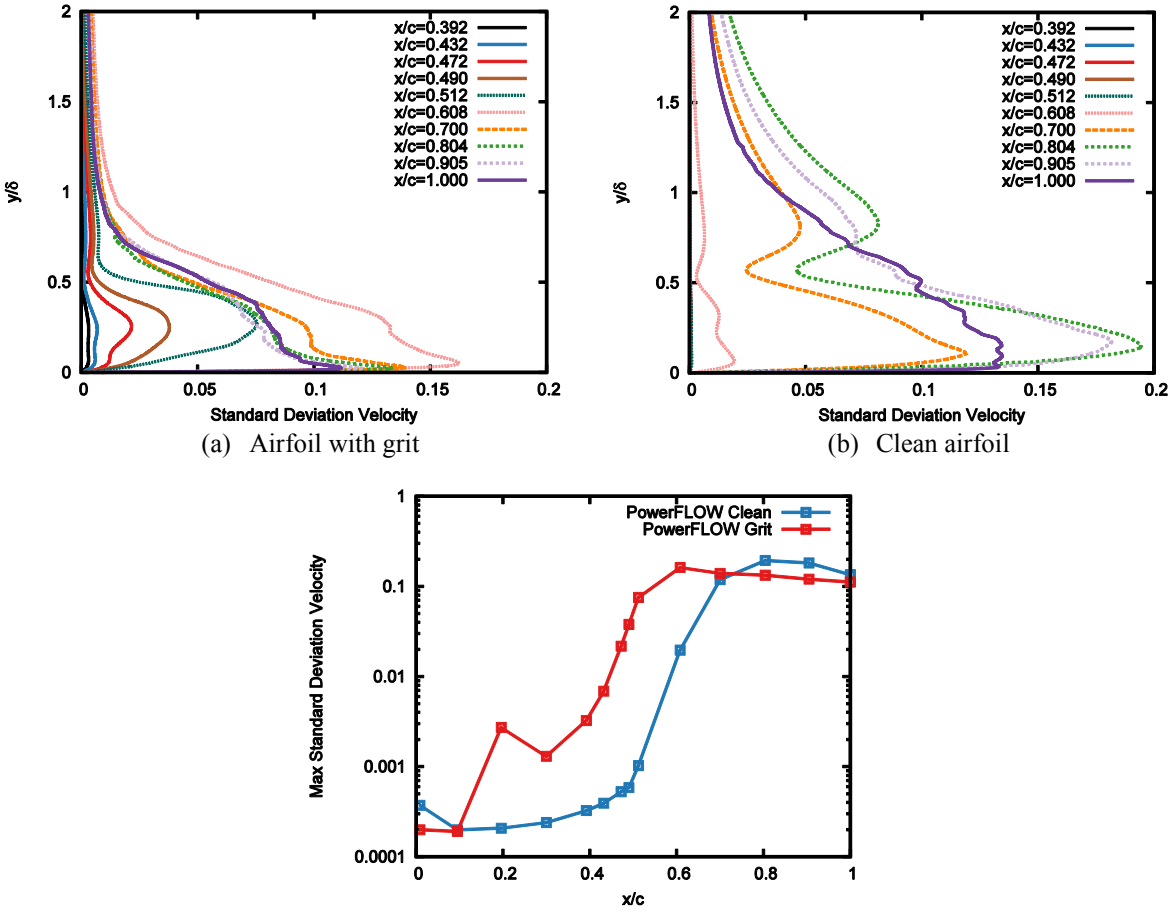

(a) Airfoil with grit

(b) Clean airfoil

(c) Maximum standard deviation velocity magnitude within different profiles along the airfoil chord

Figure 6. Velocity fluctuations normalized by freestream velocity in the boundary layer.

In the region of fully developed turbulence (x/c>0.65) in the grit case, the qualitative shape of fluctuation profiles remains similar (Figure 6(a)); however, the peak fluctuation levels decrease with increasing x/c (Figure 6(c)). The decrease in velocity fluctuation levels from x/c=0.7 to x/c=1.0 is presumably associated with the deceleration of the inviscid flow near the edge of the mean boundary layer. In contrast, the shape of velocity fluctuation profiles continues to evolve all the way up to the trailing edge in the clean airfoil case. Figure 6(b) indicates that the fluctuations in the clean case extend outside of the edge of the mean boundary layer (y/δ>1). This is likely due to the structures seen in Figure 5(b) growing in size and having an irrotational tail outside of the boundary layer.

Figure 7 shows the surface pressure spectra over the airfoil chord. The grit case displays the following behavior: at about 15% chord, a spectral peak appears at a frequency of around 10 kHz. Based on the chordwise amplification of velocity fluctuations as seen earlier in Figure 6(c), one expects this peak to be associated with the instabilities of the underlying boundary layer. At downstream locations, the spectral peak shifts to progressively lower frequencies, a trend that is qualitatively consistent with the thickening of the mean boundary layer. Across the chordwise interval of x/c=(0.3, 0.4), the contour color associated with this peak changes from green to orange, highlighting the rapid growth of these fluctuations in a frequency band that is centered near 2200 to 3400 Hz. Near 50% of the chord, the spectrum broadens rather rapidly to cover the entire frequency range, indicating a significant change in the state of the boundary layer. Based on the mean skin friction evolution in Figure 4(a), the spectral broadening appears to be associated with the

onset of transition. The highest pressure fluctuations occur within the laminar breakdown region between approximately *x/c*=(0.5, 0.6), and the spectrum appears to have filled the entire frequency range, indicating the creation of structures that span a wide range of sizes. The overshoot in spectral levels subsides when the flow becomes fully turbulent and the spectral distribution downstream of *x/c*=0.6 appears to remain mostly visually uniform on the scale of this logarithmic plot. The clean case has a different behavior, with similar peak frequencies over the entire laminar region, with the most prominent peak at approximately 1800 Hz. At 65% of the chord, high amplitude broadband fluctuations begin as indicated by dark red contour levels, but these are limited to frequencies between 600 and 5000 Hz, while the levels at frequencies higher than 10 kHz remain noticeably lower than they are in the grit case. The peak levels shown in red parallel the behavior seen in Figure 5, where large structures that appear in the boundary layer have non-uniform chordwise spacing, but do not break up into turbulence until near the TE. In other words, these peaks are not tonal and remain confined to low to intermediate frequencies within the plot. The spectra begin to show broadband behavior relatively far downstream, close to 85% of the chord, with colors shifting to orange at the highest frequencies plotted. This shift occurs around 55% chord in the grit case. The rise in high frequency fluctuations correlates to the rise in skin friction seen in Figure 4(a), indicating it is related to the transition into turbulence.

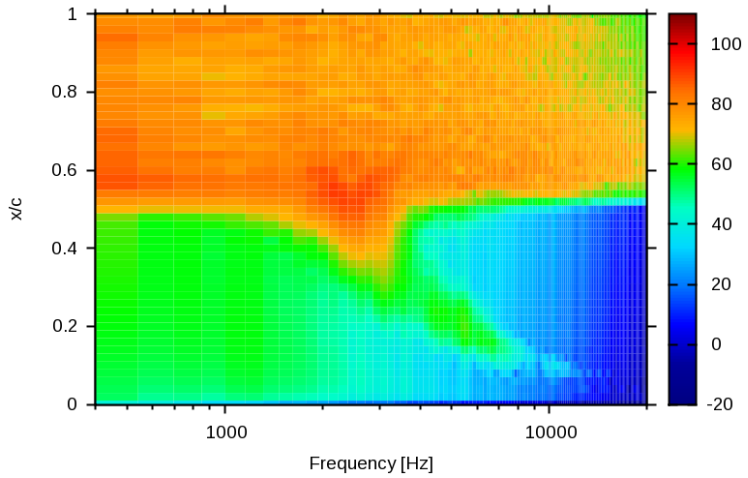

(a) Airfoil with grit

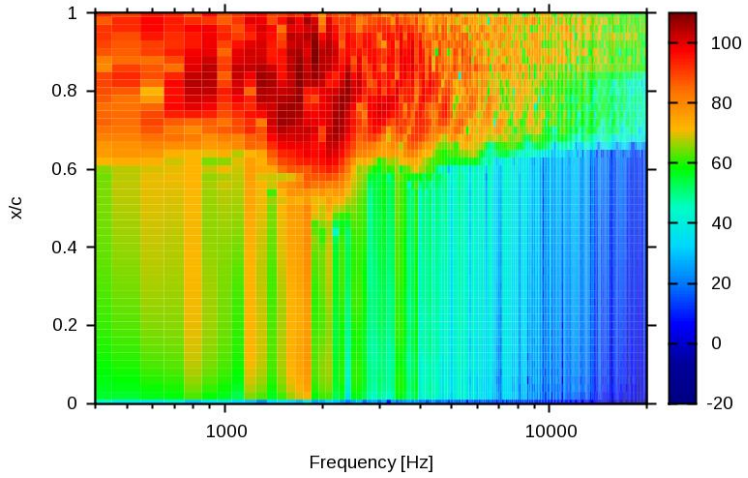

(b) Clean airfoil

Figure 7. Wall pressure spectra (dB/Hz) along the upper surface of the airfoil.

Acoustic predictions

Figure 8 shows wall pressure spectra at three chordwise locations within the turbulent portion of the airfoil surface. The computed spectra for the grit case are compared to the predictions based on the semi-empirical models of Rozenberg et al. (2012) and Schlinker and Amiet (1981). Using input specification of local boundary layer properties, namely, δ, δ^*, θ, the velocity at δ, skin friction coefficient, and the local chordwise pressure gradient, these models predict the surface pressure spectrum. The simulation results show the following trend: at x/c=0.7 the levels are 2–3 dB higher than those at the other points for nearly all frequencies. At x/c=0.8, the levels are 1–2 dB higher than those at x/c=0.9 for frequencies higher than 3 kHz and are generally similar for frequencies less than 1–2 kHz. The Rozenberg model seems to agree qualitatively with the aforementioned differences in spectral levels at the above three locations, but show significant quantitative differences in terms of absolute values, especially at x/c=0.7. The Schinkler model generally predicts lower amplitudes than those in the numerical simulations and the Rozenberg model. The qualitative trend is also different from the latter two results in that the spectral levels at x/c=0.7 as predicted by the Schinkler model are generally lower than the corresponding predictions at the other two points. The differences between the computed results and the predictions of the Rozenberg model in regard to both spectral trend at high frequencies and the overall level is attributed to the uncertainties associated with the boundary layer parameters that are required as input to evaluate the model-based spectra, in particular, the boundary layer thickness parameters and the skin friction coefficient. However, the different trends at the low-frequency end of the spectrum are more likely due to other causes. One explanation could be that, in the present transitional case, low-frequency spectral components do not have a local character due to boundary layer velocity fluctuations, but are contaminated by phenomena occurring elsewhere on the airfoil, such as acoustic fluctuations generated in the transition region. This effect can be magnified by the quasi-two-dimensional character of the present simulation with periodicity boundary conditions. Further analyses will be conducted in the future to shed further light on this feature of the computed wall pressure spectrum.

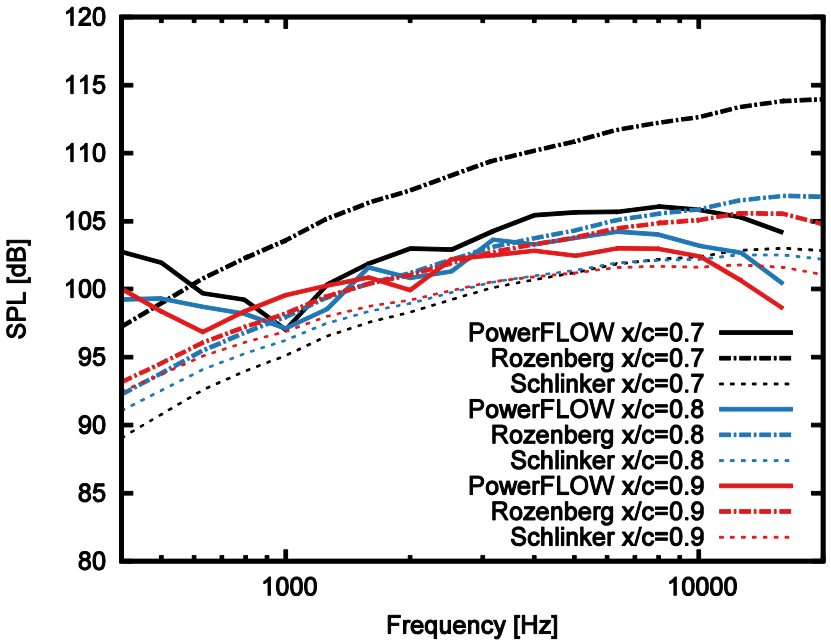

Figure 8. Wall pressure spectra for the grit case.

Figure 9 shows the spanwise pressure coherence, computed as the squared magnitude of the cross-spectrum of two points, divided by the power spectrum of both signals for given frequencies, at the TE across the airfoil span for the case with grit. The center of the TE is taken as the reference signal. Frequencies around

1 kHz show high spanwise coherence across the span. As seen in Figure 10, these frequencies are associated with the spectral peak of the TE noise. In general, Figure 9 indicates that the span used in the current simulations may be too short, since only frequencies higher than 2 kHz reach a coherence of less than 0.2 across the half width of the span. Furthermore, the asymmetry of the plot across zero spanwise separation indicates the need to acquire significantly longer sampling duration to achieve a statistically converged coherence distribution.

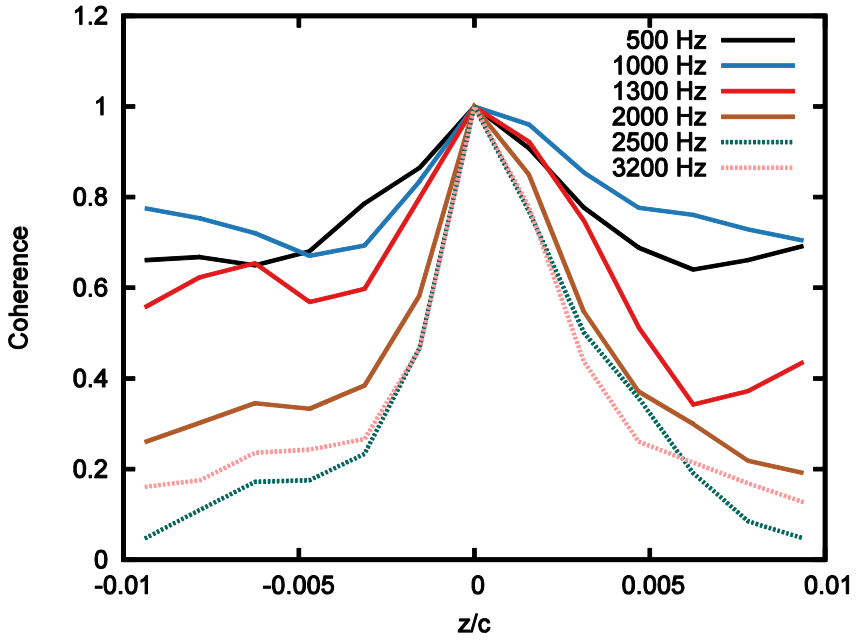

Figure 9. Pressure coherence along the span of the airfoil TE for the grit case.

Figure 10 shows the acoustic predictions at an observer location 4 chords below the TE, comparing them with the measurements by Brooks et al. (1989). Two different predictions are shown, one based on the solid FW-H approach and a semi-analytical method based on the wall pressure spectrum near the TE (Roger and Moreau, 2005), labeled as R&M. The FW-H takes as input the time history of pressure on the whole airfoil surface, while the semi-analytical approach requires the pressure PSD at the TE only. The ratio between the span of the experiments (s_e) and the span of the simulations (s_s) is used to correct the predicted sound pressure levels by adding 10 $\log_{10}(s_e/s_s)$ to the FW-H spectra. This correction is appropriate when the spanwise domain is large enough to capture the spanwise coherence length associated with the noise source. As discussed in the context of Figure 9, this requirement is not met in the present simulation at lower frequencies ($f < 2000$ Hz) and, therefore, the FW-H prediction is likely to change if the spanwise domain length is increased. On the other hand, the spanwise coherence in the R&M case is modeled using a Corcos' model with a proportionality constant between the spanwise correlation length and the ratio between the convection velocity and the radian frequency equal to b_c=1.5, and therefore, is relatively uninfluenced by the short spanwise width of the simulation domain.

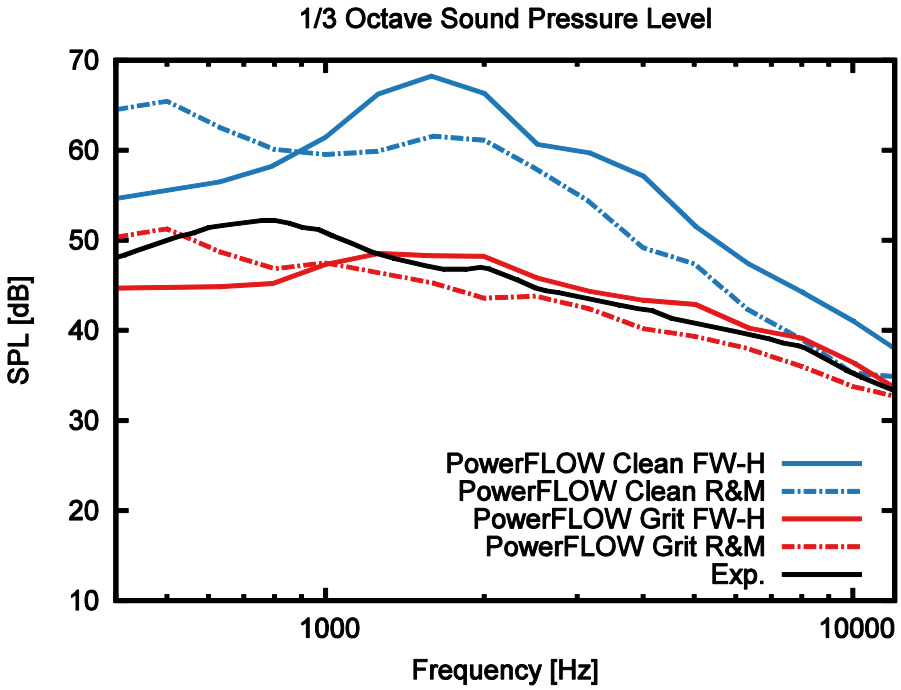

Figure 10. Farfield sound pressure levels.

The noise in the clean case (blue curve in Figure 10) is significantly higher than that in the tripped configuration and a broad peak can be observed in the clean airfoil spectrum around 1800 Hz, which corresponds to the peaks observed in the wall pressure spectra from Figure 7. The higher acoustic levels in the clean case are consistent with the higher level of surface pressure fluctuations near the trailing edge as well as with the higher spanwise coherence of those fluctuations, seen in Figure 5(b). The spanwise coherence of the input pressures is particularly high in the FW-H prediction because of the short spanwise domain, whereas the spanwise coherence in the semi-analytical result is based on the same value of the spanwise correlation coefficient b_c=1.5 as that in the grit cases. However, the quasi two-dimensional character of the turbulent flow structures predicted for the clean case would actually require a higher value of the spanwise correlation coefficient.

The acoustic predictions for the grit case match quite well the experiments of Brooks et al. (1989), with some deviations around the highest amplitude. The semi-analytical results match the grit FW-H results very well in frequencies above 1 kHz and show some differences at lower frequencies. As for the clean case, the grit case shows FW-H predictions at frequencies above 1 kHz that are consistently higher than the semi-analytical prediction by approximately 3 dB. Again, this can be due to the insufficient spanwise extent of the simulation. The disagreement at low frequencies between the FW-H and semi-analytical predictions for the grit case can be partially due to the approximate nature of the semi-analytical procedure, wherein the leading-edge back scattering correction is applied only once.

In order to do a better comparison to experiments, the TE properties should be taken into account, as they are quite different between the current results and the experimental data used in Figure 10. The report by Brooks et al. (1989) contains farfield noise for four different flow velocities, three of them higher than the one used in this work. A higher velocity means a higher *Re*, which in turn means a lower δ, which would approach the boundary layer thickness in the current simulations. Different spectra at several Mach numbers and with different values of δ can be normalized with the following equations (Herr and Reichenberger, 2011):

$$SPL_{norm} = SPL - 50\log(M) - 10\log(\delta s_e/r^2)\,, f_{norm} = f\delta/U \quad (5)$$

where M is the freestream Mach number, r is the distance to the microphone, U is the freestream velocity, and δ is the boundary layer thickness at the TE. The Mach number correction comes from the theoretical result of Ffowcs Williams and Hall (1970), according to which the farfield TE noise scales with M^5, while the frequency scaling is simply a Strouhal number conversion with δ as the characteristic length. These relations can be used to compare the acoustic spectra at different flow conditions. This is done in Figure 11, where all four velocities used by Brooks are compared with the current FW-H results for the grit case. All measured results are collapsed to the Mach number and δ values from the simulations. The measurement case with U=31.7 m/s has the same Re as the simulations and the case with U=39.6 m/s has the same M. As explained in section 2, the current simulations had an elevated M and lower Re to reduce the CPU costs. Figure 11 shows that some of the experiments have smoother spectra than others and that the current simulations seem closer to the case U=31.7 m/s than U=39.6 m/s, which was used in Figure 10. To assess the statistical convergence of the acoustic predictions based on FW-H, the plot also includes FW-H predictions based on a shorter sampling duration, corresponding to the second half of the acquisition time used in all of the analysis so far. Only small differences are seen when comparing the predictions based on both sampling intervals, indicating acceptable statistical convergence.

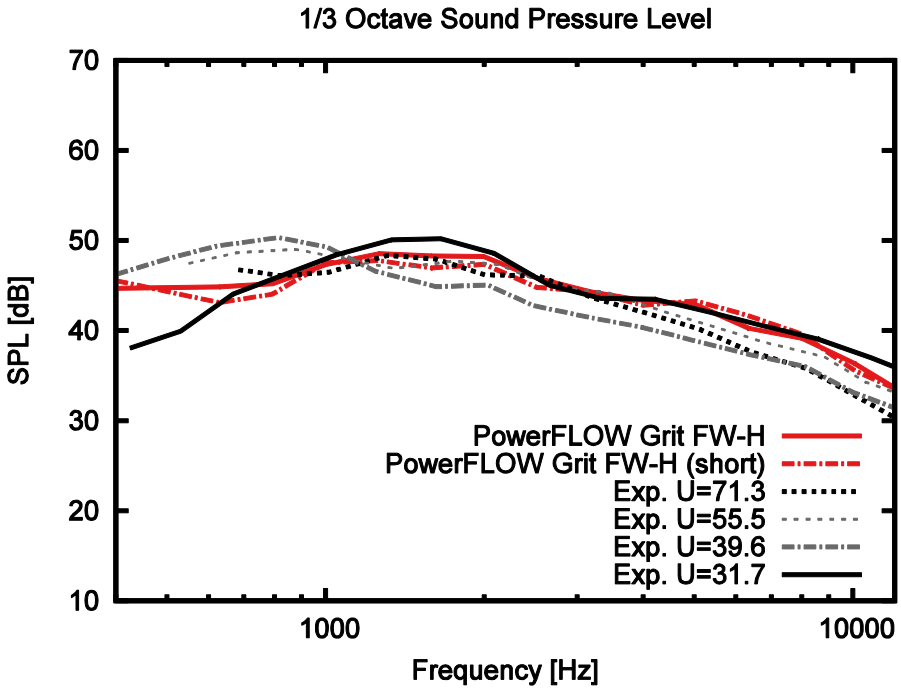

Figure 11. Comparison of FW-H predictions for acoustic spectra with measured data for different freestream velocities (in m/s). All acoustic spectra are normalized to the simulation flow conditions.

The lack of a clear peak corresponding to the TE vortex shedding in the spectra can be explained by looking at the results in Figure 12. It shows the dilatation fields for the grit case at two different time steps. At the time instant corresponding to Figure 12(a), the sound waves around the mid-chord location are much lower in amplitude than those in Figure 12(b). The images also show a lack of homogeneous spacing between the peaks and valleys of the pressure waves, which explains the aforementioned lack of peak in the spectra. Such intermittent behavior could be related to similar movement of the transition point, and will be the topic of further research in the future.

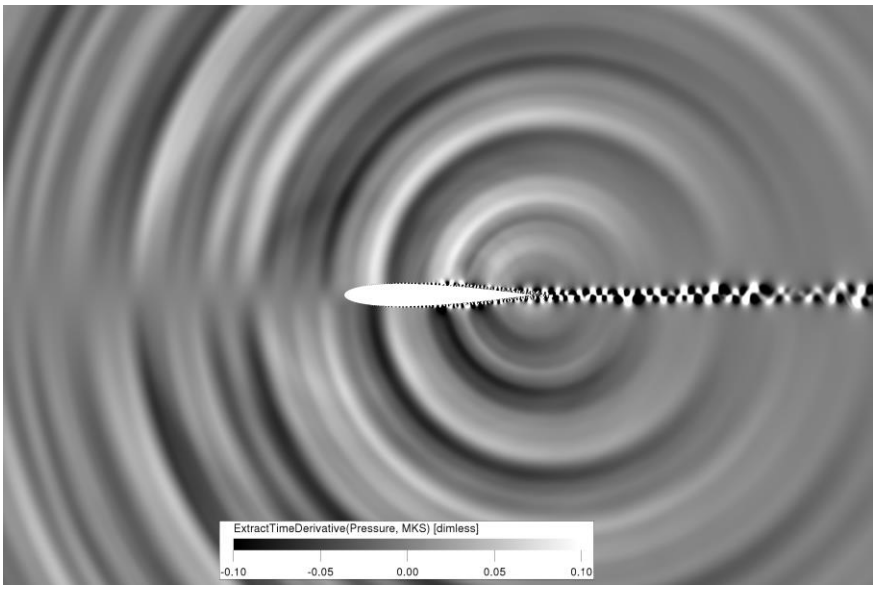

(a) Time equal to 0.0408 s

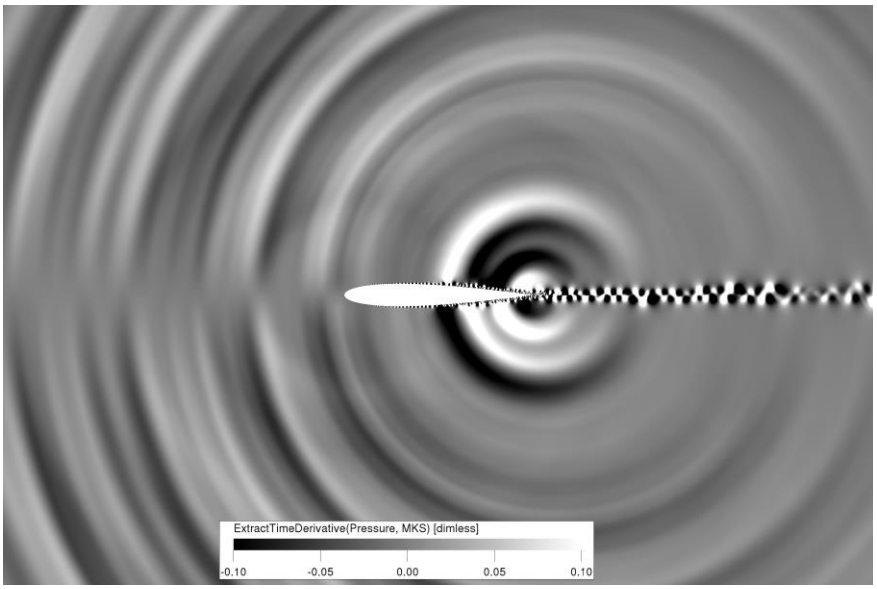

(b) Time equal to 0.0415 s

Figure 12. Dilatation mid-plane for the grit case at two timesteps.

Finally, Figure 13 shows the effect of running the simulation in single versus double precision. The top half of the image represents the double precision run with grit (i.e., the run that was the focus of this entire section), while the bottom half shows a preliminary run using single precision. The bottom half shows several vertical wave fronts superimposed on the cylindrical waves emanating from the trailing edge. The vertical fronts represent spurious acoustic waves that are generated near the outlet and propagate upstream within the computational domain. Because the noise levels associated with trailing edge noise are relatively low, the spurious acoustic waves become visible in the single precision calculation. Their amplitude is substantially lower in the double precision case, which displays a clean acoustic field centered on the trailing edge. The comparison in Figure 13 highlights the need for double precision computations for flow configurations with relatively weak noise sources.

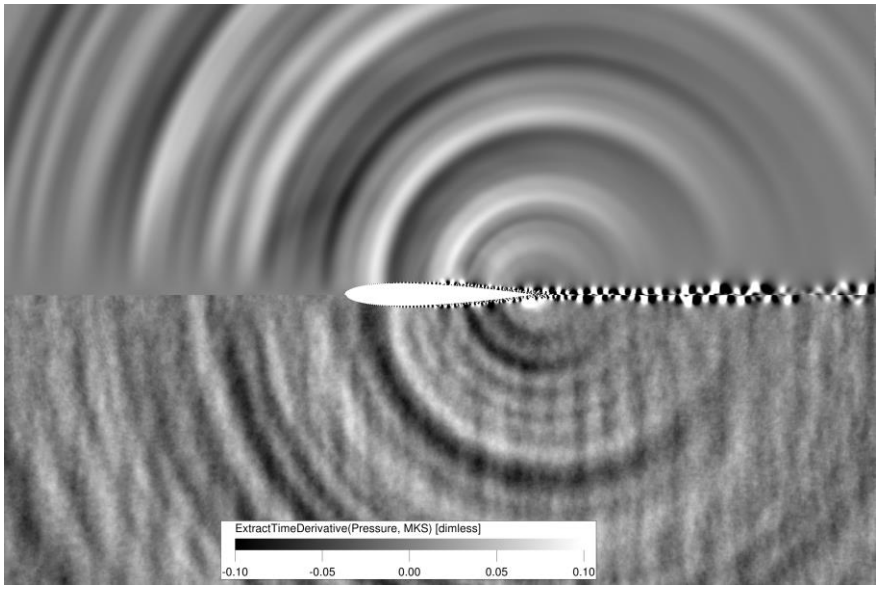

Figure 13. Dilatation mid-plane for the grit case with single (bottom half) and double (top half) precision.

4. Concluding Remarks

The present simulations based on the Lattice-Boltzmann solver PowerFLOW represent the initial phase of an ongoing effort that seeks to extend the state of the art in the numerical simulation of trailing edge noise in three different ways. First, DNS of self-noise are extended to a significantly higher Reynolds number of 0.657 million, indicating good preliminary comparisons with the measured data. Second, the DNS extends a single previous LES in modeling the process of boundary layer transition due to surface mounted trip(s) in airfoil-self-noise experiments. Third, and most important, transition in the presence of distributed surface roughness in the form of sand grain roughness near the leading edge has been modeled for possibly the first time in the context of an airfoil flow field. To make these advances possible during this initial, proof-of-concept study, certain compromises had to be made, which should be examined and improved upon during the follow-on work. One notable shortcoming pertains to grid convergence with respect to spatial resolution and the extent of spanwise domain, which could not be investigated due to a lack of sufficient computational resources. Second, the modeling of sandgrain roughness needs improvement to better mimic the characteristics of the grit on wind tunnel models. In particular, the present simulations were based on 50 percent penetration depth of the grit, which is too large for typical wind tunnel articles. Also, the grit used in wind tunnel experiments (typically made of silicon carbide or aluminum oxide) is not spherical in shape. Thus, geometric fidelity to actual grit is another area that requires further attention. Finally, the physical mechanisms underlying the transition process should also be investigated in future work. Specifically, there is a need to establish the origin of the unsteady disturbances underlying the transition process, i.e., whether they originate due to absolute instabilities related to the presence of the roughness, or to feedback processes associated with scattering near the trailing edge, to vortex shedding at the trailing edge, or to numerical noise in the discrete simulation, is not clear at the present time, although the fact that the transition location was nearly the same for a symmetric simulation in single precision partially addresses the latter. Neither of the previous simulations of trailing edge noise involving boundary layer transition (whether due to a physical trip or a numerical device) have addressed the important topic of the origin of the unsteady disturbances.

Additional efforts are currently underway to assess an alternate, hybrid simulation approach that would capture the effects of sandgrain roughness with DNS, but relax the resolution requirements in the aft region to provide a substantially more efficient simulation based on wall modeled simulations of the fully turbulent

region. The full DNS simulations of the type described herein will provide a valuable reference to evaluate and improve the hybrid approach that is better suited for practical applications involving the need to directly simulate the transition mechanism.

References

Amiet, R.K., 1976. Noise due to Turbulent Flow Past a Trailing Edge. *Journal of Sound and Vibration* 47 (3), 387-393.

Barbarino, M., Casalino, D., 2012. Hybrid Analytical/Numerical Prediction of Propeller Broadband Noise in the Time Domain. *International Journal of Aeroacoustics* 11 (2), 157-175.

Bertagnolio, F., 2012. Improved Trailing Edge Noise Model. *EUDP Project: Low Noise Airfoil - Final Report*, 30-35.

Bhatnagar, P.L., Gross, E.P., Krook, M., 1954. A Model for Collision Processes in Gases. I. Small Amplitude Processes in Charged and Neutral One-Component Systems. *Physical Review* 94 (3), 511-525.

Brooks, T.F., Hodgson, T.H., 1981. Trailing Edge Noise Prediction from Measured Surface Pressures. *Journal of Sound and Vibration* 78 (1), 69-117.

Brooks, T.F., Pope, D.S., Marcolini, M.A., 1989. Airfoil Self-Noise and Prediction. *NASA Reference Publication* 1218.

Casalino, D., 2003. An Advanced Time Approach for Acoustic Analogy Predictions. *Journal of Sound and Vibration* 261 (4), 583-612.

Casalino, D., Barbarino, M., 2011. Stochastic Method for Airfoil Self-Noise Computation in Frequency Domain. *AIAA Journal* 49 (11), 2453-2469.

Casalino, D., Noelting, S., Fares, E., Van de Ven, T., Pérot, F., Brès, G., 2012. Towards Numerical Aircraft Noise Certification: Analysis of a Full-Scale Landing Gear in Fly-Over Configuration. *AIAA Paper* 2012-2235.

Chapman, S., Cowling, T., 1990. *The Mathematical Theory of Non-Uniform Gases*, Cambridge University Press, London.

Chase, D.M., 1975. Noise Radiated from an Edge in Turbulent Flow. *AIAA Journal* 13, 1041-1047.

Chase, D.M., 1980. Modeling the Wavevector-Frequency Spectrum of Turbulent Boundary Layer Wall Pressure. *Journal of Sound and Vibration* 70 (1), 29-67.

Chen, H., Chen, S., Matthaeus, W.H., 1992. Recovery of the Navier-Stokes Equations Using a Lattice-Gas Boltzmann Method. *Physical Review A* 45 (8), 5339-5342.

Chen, H., Kandasamy, S., Orszag, S., Shock, R., Succi, S., Yakhot, V., 2003. Extended Boltzmann Kinetic Equation for Turbulent Flows. *Science* 301 (5633), 633-636.

Chen, H., Teixeira, C., 2000. H-Theorem and Origins of Instability in Thermal Lattice Boltzmann Models. *Computer Physics Communications* 129, 21-31.

Chen, H., Teixeira, C., Molvig, K., 1997. Digital Physics Approach to Computational Fluid Dynamics: some basic theoretical features. *International Journal of Modern Physics C* 8 (4), 675-684.

Chen, H., Teixeira, C., Molvig, K., 1998. Realization of Fluid Boundary Conditions via Discrete Boltzmann Dynamics. *International Journal of Modern Physics C* 9 (8), 1281-1292.

Chen, S., Doolen, G.D., 1998. Lattice Boltzmann Method for Fluid Flows. *Annual Review of Fluid Mechanics* 30, 329-364.

Choudhari, M., Bahr, C., Khorrami, M.R., Lockard, D.P., Lopes, L., Zawodny, N., Herr, M., Pott-Pollenske, M., Kamruzzaman, M., Van de Ven, T., Manoha, E., Redonnet, S., Yamamoto, K., Ikeda, I., Imamura, T., 2016. Simulations & Measurements of Airframe Noise: A BANC Workshops Perspective. *Proceedings of NATO STO-MP-AVT-246 Specialists Meeting on Progress and Challenges in Validation Testing for Computational Fluid Dynamics*, Avila, Spain, Sept. 26-28.

Courant, R., Friedrichs, K., Lewy, H., 1928. Über die partiellen Differenzengleichungen der mathematischen Physik. *Mathematische Annalen* 100 (1), 32-74.

Dassen, T., Parchen, R., Bruggeman, J., Hagg, F., 1996. Results of a wind tunnel study on the reduction of airfoil self-noise by the application of serrated blade trailing edges. *Technical Report*, National Aerospace Laboratory NLR, NLR-TP-96350.

Drela, M., 1989. XFOIL: An Analysis and Design System for Low Reynolds Number Airfoils. *Conference on Low Reynolds Number Airfoil Aerodynamics*. University of Notre Dame.

Ewert, R., Appel C., Dierke, J., Herr, M., 2009. RANS/CAA Based Prediction of NACA0012 Broadband Trailing Edge Noise and Experimental Validation. AIAA Paper 2009-3269.

Fan, H., Zhang, R., Chen, H., 2006. Extended Volumetric Scheme for Lattice Boltzmann Models. *Physical Review E* 73, 066708.

Farassat, F., Succi, G.P., 1983. The Prediction of Helicopter Discrete Frequency Noise. *Vertica* 7 (4), 309-320.

Ffowcs Williams, J.E., Hall, L.H., 1970. Aerodynamic Sound generation by Turbulent Flow in the Vicinity of a Scattering Half-Plane. *Journal of Fluid Mechanics* 40, 657-670.

Garcia-Sagrado, A., Hynes, T., 2012. Wall Pressure Sources Near an Airfoil Trailing Edge Under Turbulent Boundary Layers. *Journal of Fluids and Structures* 30, 3-34.

George, J.K., Lele, S., 2016. Large Eddy Simulation of Airfoil Self-Noise at High Reynolds Number. AIAA Paper 2016-2919.

Gershfeld, J., Blake, W.K., Knisely, C.W., 1988. Trailing Edge Flows and Aerodynamic Sound. AIAA Paper 88-3826.

Gloerfelt, X., Le Garrec, T., 2009. Trailing Edge Noise from an Isolated Airfoil at a High Reynolds Number. AIAA Paper 2009-3201.

Goody, M., 2004. Empirical Spectral Model of Surface Pressure Fluctuations. *AIAA Journal* 42 (9), 1788-1794.

Gruber, M., Azarpeyvand, M., Joseph, P., 2010. Airfoil Trailing Edge Noise Reduction by the Introduction of Sawtooth and Slitted Trailing Edge Geometries. *Proceedings of 20th International Congress on Acoustics*, ICA2010, 23-27 August, Sydney, Australia.

Herr, M., Dobrzynski, W., 2005. Experimental Investigations in Low-Noise Trailing-Edge Design. *AIAA Journal* 43 (6), 1167-1175.

Herr, M., Ewert, R., Rautmann, C., Kamruzzaman, M., Bekiropoulos, D., Iob, A., Arina, R., Batten, P., Chakravarthy, S., Bertagnolio, F., 2015. Broadband Trailing-Edge Noise Predictions Overview of BANC-III Results. AIAA Paper 2015-2847.

Herr, M., Kamruzzaman, M., 2013. Benchmarking of Trailing-Edge Noise Computations|Outcome of the BANC-II Workshop, AIAA Paper 2013-2123.

Herr, M., Reichenbergern J., 2011. In Search of Airworthy Trailing-Edge Noise Reduction Means. AIAA Paper 2011-2780.

Herrig, A., 2011. Validation and Application of a Hot-Wire Based Method for Trailing-Edge Noise Measurements on Airfoils. Doctoral thesis, Institute of Aerodynamics and Gas Dynamics, Faculty of Aerospace Engineering and Geodesy, University of Stuttgart, Stuttgart, Germany.

Howe, M.S., 1978. A Review of the Theory of Trailing-Edge Noise. *Journal of Sound and Vibration* 61 (3), 437-465.

Howe, M.S., 1998. *Acoustics of Fluid-Structure Interactions*. Cambridge University Press, New York, 204-209.

Hutcheson, F.V., Brooks, T.F., 2002. Measurement of Trailing Edge Noise Using Directional Array and Coherent Output Power Methods. *International Journal of Aeroacoustics* 1 (4), 329–353.

Iob, A., Arina, R., Batten, P., Chakravarthy, S., 2014. Generating Trailing-Edge Noise Predictions Using Synthetic Turbulence. AIAA Paper 2014-2764.

Jeong, J., Hussain, F., 1995. On the Identification of a Vortex. *Journal of Fluid Mechanics* 285, 69-94.

Jones, L., Sandham, N., Sandberg, R., 2010, Acoustic Source Identification for Transitional Airfoil Flows Using Crosscorrelations, *AIAA Journal* 48 (10).

Keith, W.L., Hurdis, D.A., Abraham, B.M., 1992. A Comparison of Turbulent Boundary Layer Wall-Pressure Spectra. *Journal of Fluids Engineering* 114 (3), 338-347.

Koenig, B., Fares, E., Ishikawa, K., Murayama, M., Ito, Y., Yokokawa, Y., Yamamoto, K., 2016. Lattice-Boltzmann Simulations of the JAXA JSM High-Lift Model. AIAA Paper 2016-3721.

Langtry, R. B., Menter, F. R., 2009. Correlation-Based Transition Modeling for Unstructured Parallelized Computational Fluid Dynamics Codes. *AIAA Journal* 47 (12), 2894-2906.

Li, Y., Shock, R., Zhang, R., Chen, H., 2004. Numerical Study of Flow Past an Impulsively Started Cylinder by Lattice Boltzmann Method. *Journal of Fluid Mechanics* 519, 273-300.

Lin, Y., Savill, M., Vadlamani, N.R., Jefferson-Love Day, R., 2013. Wall-Resolved Large Eddy Simulation over NACA0012 Airfoil. *International Journal of Aerospace Sciences*, 2 (4), 149-162.

Manoha, E., Troff, B., Sagaut, P., 2000. Trailing-Edge Noise Prediction Using Large-Eddy Simulation and Acoustic Analogy. *AIAA Journal* 38, 575-583.

Marsden, O., Bogey, C., Bailly, C., 2008. Direct Noise Computation of the Turbulent Flow Around a Zero-Incidence Airfoil. *AIAA Journal* 46, 874-883.

Migliore, P., Oerlemans, S., 2004. Wind Tunnel Aeroacoustic Tests of Six Airfoils for Use on Small Wind Turbines. *Journal of Solar Energy Engineering* 126 (4), 974-985.

Oberai, A.A., Roknaldin, F., Hughes, T.J.R., 2002. Computation of Trailing-Edge Noise Due to Turbulent Flow Over an Airfoil. *AIAA Journal* 40 (11), 2206-2216.

Oerlemans, S., Sijtsma, P., Méndez López, B., 2006. Location and Quantification of Noise Sources on a Wind Turbine. *Journal of Sound and Vibration* 299 (4-5), 869-883.

Park, I., Moin, P., 2016. Space-Time Characteristics of Wall-Pressure and Wall Shear-Stress Fluctuations in Wall-Modeled Large Eddy Simulation. *Physical Review Fluids* 1, 024404.

Qian, Y.H., D'Humières, D., Lallemand, P., 1992. Lattice BGK Models for Navier-Stokes Equation. *Europhysics Letters* 17 (6), 479-484.

Ribeiro, A.F.P., Casalino, D., Fares, E., 2016. Lattice-Boltzmann Simulations of an Oscillating NACA0012 Airfoil in Dynamic Stall. In Braza, M., Bottaro, A., Thompson, M. ed., *Advances in Fluid-Structure Interaction*, Springer, 179-192.

Roger, M., Moreau, S., 2005. Back-Scattering Correction and Further Extensions of Amiet's Trailing Edge Noise Model. Part 1: Theory. *Journal of Sound and Vibration* 286 (3), 477-506.

Rozenberg, Y., Robert, G., Moreau, S., 2012. Wall-Pressure Spectral Model Including the Adverse Pressure Gradient Effects. *AIAA Journal* 50 (10), 2168-2179.

Rozenberg, Y., Roger, M., Moreau, S., 2008. Fan Blade Trailing-Edge Noise Prediction Using RANS Simulations. *The Journal of the Acoustical Society of America* 123, 3688.

Sanjosé, M., Méon, C., Masson, V., Moreau, S., 2014. Direct Numerical Simulation of Acoustic Reduction Using Serrated Trailing-Edge on an Isolated Airfoil. AIAA Paper 2014-2324.

Schinkler, R.H., Amiet, R.K., 1981. Helicopter Rotor Trailing Edge. NASA Technical Report CR-3470.

Schlichting, H., Gersten, K., 2000. *Boundary Layer Theory*. 8th edition. Berlin Heidelberg: Springer-Verlag.

Shan, X., Yuan, X.-F., Chen, H., 2006. Kinetic Theory Representation of Hydrodynamics: A Way Beyond the Navier-Stokes Equation. *Journal of Fluid Mechanics* 550, 413-441.

Slotnick, J., Khodadoust, A., Alonso, J., Darmofal, D., Gropp, W., Lurie, E., Mavriplis, D., 2014. CFD Vision 2030 Study: A Path to Revolutionary Computational Aerosciences. *NASA Technical Report*, CR-2014-218178.

Wang, M., Moin, P., 2000. Computation of Trailing-Edge Flow and Noise Using Large-Eddy Simulation. *AIAA Journal* 38, 2201-2209.

Winkler, J., Moreau, S., Carolus, T., 2009. Large-Eddy Simulation and Trailing-Edge Noise Prediction of an Airfoil with Boundary-Layer Tripping. AIAA Paper 2009-3197.

Winkler, J., Moreau, S., Carolus, T., 2012. Airfoil Trailing-Edge Blowing: Broadband Noise Prediction from Large-Eddy Simulation. *AIAA Journal* 50, 294-303.

Wolf, W.R., Lele, S.K., 2012. Trailing-Edge Noise Predictions Using Compressible Large-Eddy Simulation and Acoustic Analogy. *AIAA Journal* 50, 2423-2434.

REPORT DOCUMENTATION PAGE

Form Approved
OMB No. 0704-0188

1. REPORT DATE *(DD-MM-YYYY)*	2. REPORT TYPE	3. DATES COVERED *(From - To)*
01-12-2016	Technical Memorandum	

4. TITLE AND SUBTITLE

Direct Numerical Simulation of an Airfoil With Sand Grain Roughness on the Leading Edge

5a. CONTRACT NUMBER

5b. GRANT NUMBER

5c. PROGRAM ELEMENT NUMBER

6. AUTHOR(S)

Ribeiro, Andre F. P.; Casalino, Damiano; Fares, Ehab; Choudhari, Meelan M.

5d. PROJECT NUMBER

5e. TASK NUMBER

5f. WORK UNIT NUMBER

01876.02.07.03.01.02

7. PERFORMING ORGANIZATION NAME(S) AND ADDRESS(ES)

NASA Langley Research Center
Hampton, VA 23681-2199

8. PERFORMING ORGANIZATION REPORT NUMBER

L-20774

9. SPONSORING/MONITORING AGENCY NAME(S) AND ADDRESS(ES)

National Aeronautics and Space Administration
Washington, DC 20546-0001

10. SPONSOR/MONITOR'S ACRONYM(S)

NASA

11. SPONSOR/MONITOR'S REPORT NUMBER(S)

NASA-TM-2016-219363

12. DISTRIBUTION/AVAILABILITY STATEMENT

Unclassified - Unlimited
Subject Category 02
Availability: NASA STI Program (757) 864-9658

13. SUPPLEMENTARY NOTES

14. ABSTRACT

As part of a computational study of acoustic radiation due to the passage of turbulent boundary layer eddies over the trailing edge of an airfoil, the Lattice-Boltzmann method is used to perform direct numerical simulations of compressible, low Mach number flow past an NACA 0012 airfoil at zero degrees angle of attack. The chord Reynolds number of approximately 0.657 million models one of the test conditions from a previous experiment by Brooks, Pope, and Marcolini at NASA Langley Research Center. A unique feature of these simulations involves direct modeling of the sand grain roughness on the leading edge, which was used in the abovementioned experiment to trip the boundary layer to fully turbulent flow. This report documents the findings of preliminary, proof-of-concept simulations based on a narrow spanwise domain and a limited time interval. The inclusion of fully-resolved leading edge roughness in this simulation leads to significantly earlier transition than that in the absence of any roughness. The simulation data is used in conjunction with both the Ffowcs Williams-Hawkings acoustic analogy and a semi-analytical model by Roger and Moreau to predict the farfield noise.

15. SUBJECT TERMS

Boltzmann; Boundary layer; Computational study; Mach number; Reynolds

16. SECURITY CLASSIFICATION OF:			17. LIMITATION OF ABSTRACT	18. NUMBER OF PAGES	19a. NAME OF RESPONSIBLE PERSON
a. REPORT	b. ABSTRACT	c. THIS PAGE			STI Help Desk (email: help@sti.nasa.gov)
U	U	U	UU	31	19b. TELEPHONE NUMBER *(Include area code)* (757) 864-9658